Original citation:
Armstrong, David J., Pugh, C. E., Broomhall, A. -M., Brown, D. J. A., Lund, M. N., Osborn, H. P. and Pollacco, Don. (2016) The host stars of Kepler's habitable exoplanets : superflares, rotation and activity. Monthly Notices of the Royal Astronomical Society, 455 (3). pp. 3110-3125.

Permanent WRAP URL:
http://wrap.warwick.ac.uk/78564

Link to final published version: http://dx.doi.org/10.1093/mnras/stv2419

A note on versions:
The version presented in WRAP is the published version or, version of record, and may be cited as it appears here.

For more information, please contact the WRAP Team at: wrap@warwick.ac.uk

warwick.ac.uk/lib-publications

The host stars of *Kepler*'s habitable exoplanets: superflares, rotation and activity

D. J. Armstrong,[1,2]★ C. E. Pugh,[1] A.-M. Broomhall,[1] D. J. A. Brown,[1] M. N. Lund,[3] H. P. Osborn[1] and D. L. Pollacco[1]

[1]*University of Warwick, Department of Physics, Gibbet Hill Road, Coventry CV4 7AL, UK*
[2]*ARC, School of Mathematics & Physics, Queen's University Belfast, University Road, Belfast BT7 1NN, UK*
[3]*Stellar Astrophysics Centre (SAC), Department of Physics and Astronomy, Aarhus University, Ny Munkegade 120, DK-8000 Aarhus C, Denmark*

ABSTRACT

We embark on a detailed study of the light curves of *Kepler*'s most Earth-like exoplanet host stars using the full length of *Kepler* data. We derive rotation periods, photometric activity indices, flaring energies, mass-loss rates, gyrochronological ages, X-ray luminosities and consider implications for the planetary magnetospheres and habitability. Furthermore, we present the detection of superflares in the light curve of Kepler-438, the exoplanet with the highest Earth Similarity Index to date. Kepler-438b orbits at a distance of 0.166 au to its host star, and hence may be susceptible to atmospheric stripping. Our sample is taken from the Habitable Exoplanet Catalogue, and consists of the stars Kepler-22, Kepler-61, Kepler-62, Kepler-174, Kepler-186, Kepler-283, Kepler-296, Kepler-298, Kepler-438, Kepler-440, Kepler-442, Kepler-443 and KOI-4427, between them hosting 15 of the most habitable transiting planets known to date from *Kepler*.

Key words: planets and satellites: general – planets and satellites: magnetic fields – stars: activity – stars: flare – stars: rotation.

1 INTRODUCTION

In recent years the pace of discovery of exoplanets has intensified, with an increasing number of small, potentially rocky planets being found. This is largely due to the *Kepler* mission (Borucki et al. 2010; Koch et al. 2010), which studies ∼150 000 stars with high-precision photometry, and has found several thousand candidate exoplanets. With more planets comes a focus on new questions, including the potential habitability of these planets in a much more diverse range of environments than known in the Solar system.

The key driver of an exoplanet's local environment is its host star. This leads to well-known properties such as the equilibrium temperature of the exoplanet, defining the habitable zone where liquid water could exist on the planet's surface (e.g. Kasting 1993). Many of the newly discovered planets orbit stars cooler than the Sun, because around these stars habitable zone planets are often easier to detect. These stars are known to have increased activity relative to Sun-like stars (Wright et al. 2011), as well as increased potential for flaring, coronal mass ejections (CMEs), X-ray and EUV flux (Mamajek & Hillenbrand 2008), and active magnetic fields (Reiners & Mohanty 2012; Vidotto et al. 2014). Such properties tend to get weaker as a host star ages and spins-down (e.g. Hempelmann

et al. 1995; van Saders & Pinsonneault 2013; García et al. 2014, along with many others) and all have a potential effect on planetary habitability.

Stellar flares are associated with increased UV and charged particle flux, but this is thought not to affect planetary habitability (Segura et al. 2010). They are, however, also associated with increased likelihood of CMEs (Chen & Kunkel 2010), which can compress planetary magnetospheres (Khodachenko et al. 2007) and drive atmospheric erosion (Lammer et al. 2007). UV flux, whether from a flare or background stellar radiation, can affect atmospheric heating and chemistry, as well as changing the biomarkers which future missions might search for (France, Linsky & Parke Loyd 2014; Grenfell et al. 2014). Stellar activity is associated with increased flaring rates, also potentially impacting atmospheric biomarkers and in some strong cases destroying ozone, an important element in shielding the Earth from radiation (Grenfell et al. 2012).

Planetary magnetospheres are important for shielding planets from potential atmospheric erosion and from high-energy particles, with unshielded planets orbiting M dwarfs losing their atmospheres in 1 Gyr in some cases (Zendejas, Segura & Raga 2010). The size of a magnetosphere of a planet is strongly affected by the host star, in particular its stellar wind (See et al. 2014) and magnetic fields (Vidotto et al. 2013). Variations in the stellar wind can interact strongly with a planet's atmosphere, stripping it or depositing heat and gravity waves (Cohen et al. 2014, 2015). Considering the local

★ E-mail: d.j.armstrong@warwick.ac.uk

Table 1. Host star input parameters.

Star	$T_{\rm eff}$ (K)	log g (dex)	Fe/H (dex)	R_* ($R_\odot$)	M_* ($M_\odot$)	ρ_* (g cm)$^{-3}$	Source
Kepler-22	5518 ± 44	4.44 ± 0.06	-0.29 ± 0.06	0.979 ± 0.02	0.970 ± 0.06	1.46 ± 0.13^a	Borucki et al. (2012)
Kepler-61	4016^{+68}_{-150}	$4.66^{+0.08}_{-0.04}$	0.03 ± 0.14	$0.62^{+0.02}_{-0.05}$	0.635 ± 0.037	$3.76^{+0.94a}_{-0.42}$	Ballard et al. (2013)
Kepler-62	4925 ± 70	4.68 ± 0.04	-0.37 ± 0.04	0.64 ± 0.02	0.69 ± 0.02	3.72 ± 0.36^a	Borucki et al. (2013)
Kepler-174	4880 ± 126	4.679 ± 0.15	-0.43 ± 0.10	0.622 ± 0.032	0.67 ± 0.13^a	3.956 ± 0.450	Rowe et al. (2014)
Kepler-186	3755 ± 90	4.736 ± 0.02	-0.26 ± 0.12	$0.523^{+0.023}_{-0.021}$	$0.544^{+0.024}_{-0.021}$	$5.29^{+0.54}_{-0.39}$	Torres et al. (2015)
Kepler-283	4351 ± 100	4.72 ± 0.15	-0.2 ± 0.1	0.566 ± 0.024	0.61 ± 0.09^a	4.770 ± 0.403	Rowe et al. (2014)
Kepler-296	3740 ± 130	$4.774^{+0.091}_{-0.059}$	-0.08 ± 0.3	$0.48^{+0.066}_{-0.087}$	$0.498^{+0.067}_{-0.087}$	$6.4^{+3.2}_{-1.5}$	Barclay et al. (2015)
Kepler-298	4465 ± 100	4.709 ± 0.15	-0.24 ± 0.1	0.582 ± 0.025	0.63 ± 0.10^a	4.526 ± 0.414	Rowe et al. (2014)
Kepler-438	3748 ± 112	$4.74^{+0.059}_{-0.029}$	0.16 ± 0.14	$0.520^{+0.038}_{-0.061}$	$0.544^{+0.041}_{-0.061}$	$5.52^{+1.53}_{-0.77}$	Torres et al. (2015)
Kepler-440	4134 ± 154	$4.706^{+0.049}_{-0.016}$	-0.30 ± 0.15	$0.559^{+0.029}_{-0.054}$	$0.575^{+0.043}_{-0.047}$	$4.76^{+1.03}_{-0.48}$	Torres et al. (2015)
Kepler-442	4402 ± 100	$4.673^{+0.018}_{-0.021}$	-0.37 ± 0.10	$0.598^{+0.023}_{-0.024}$	$0.609^{+0.03}_{-0.026}$	$4.01^{+0.37}_{-0.30}$	Torres et al. (2015)
Kepler-443	4723 ± 100	$4.614^{+0.016}_{-0.029}$	-0.01 ± 0.10	$0.706^{+0.028}_{-0.024}$	$0.738^{+0.033}_{-0.029}$	$2.96^{+0.24}_{-0.25}$	Torres et al. (2015)
KOI-4427	3813 ± 112	$4.751^{+0.067}_{-0.030}$	-0.07 ± 0.14	$0.505^{+0.038}_{-0.065}$	$0.526^{+0.040}_{-0.062}$	$5.79^{+1.87}_{-0.82}$	Torres et al. (2015)

Note. ^{a}Derived from parameters in source paper.

galactic environment rather than the star could also have an effect; recently Johnson, Redfield & Jensen (2015) showed that variable interstellar medium density can affect the astrosphere of planetary systems, changing the level of shielding to cosmic rays.

Exoplanets are often rated on the Earth Similarity Index (ESI; Schulze-Makuch et al. 2011), which measures the similarity of a planet to Earth based on its radius, bulk density, escape velocity and surface temperature. In this work, we consider the host stars of the most Earth-like exoplanets defined by this index, as found in the Habitable Exoplanets Catalogue.[1] To allow an in-depth photometric study of this sample, we limit ourselves to stars observed by the *Kepler* mission, giving a sample of 13 stars hosting 15 highly ranked planets. The sample consisted of Kepler-22b (KIC 10593626; Borucki et al. 2012), Kepler-61b (KIC 6960913; Ballard et al. 2013), Kepler-62e and f (KIC 9002278; Borucki et al. 2013), Kepler-174d (KIC 8017703; Rowe et al. 2014), Kepler-186f (KIC 8120608; Quintana et al. 2014), Kepler-283c (KIC 10604335), Kepler-296e and f (KIC 11497958), Kepler-298d (KIC 11176127; Rowe et al. 2014), Kepler-438b (KIC 6497146), Kepler-440b (KIC 6106282), Kepler-442b (KIC 4138008), Kepler-443b (KIC 11757451) and KOI-4427b (KIC 4172805; Torres et al. 2015), where KOI stands for *Kepler* Object of Interest, and KIC represents the Kepler Input Catalogue identifier for the star. Kepler-296 is a binary system with five transiting planets. It has only recently been shown that all these planets likely orbit the same star in the binary (Barclay et al. 2015). The parameters of these stars are listed in Table 1, in some cases from a more recent source than the discovery paper.

2 DATA

All *Kepler* light curves are available publicly via the Michulski Archive for Space Telescopes. These light curves are provided both in raw format and as the detrended PDC ms-MAP light curves (Presearch Data Conditioning multi-scale Maximum A Posteriori; Smith et al. 2012; Stumpe et al. 2012), and span a range of approximately four years from 2009 May to 2013 May. We make use of

[1] http://phl.upr.edu/projects/habitable-exoplanets-catalog

the full time series, comprising quarters 0–17 (the spacecraft reorientated itself every ∼90 d, separating the data into quarters). The PDC light curves are explicitly designed to remove instrumental variability while preserving astrophysical flux variations. However, they also apply a high-pass filter to the data, effectively attenuating any signal on a time-scale longer than approximately 21 d (García et al. 2013). For work involving exoplanetary transits this usually has little effect, but for the study of long stellar rotation periods problems can be introduced. As a large part of this work derives from determinations of the host star rotation periods, we make use of the Kepler Asteroseismic Science Operations Center (KASOC) light curves. See Handberg & Lund (2014) for a detailed description of these light curves and how they are generated. These can be processed with filters of different durations, and in this work we employ light curves using filters of 30, 50, and 100 d. A shorter filter tends to produce cleaner light curves, but also attenuates signal on time-scales longer than the filter. Before any further processing, transits of the known planets are cut using their published ephemeris.

Each of the systems studied here have been investigated in depth in their respective discovery papers. Here we concentrate on the host stars, as well as the effects these may have on their orbiting planets.

3 METHODS

3.1 Rotation periods

Several of the target stars already have determinations of the rotation period. These were generally performed using PDC data, which as described above can lead to problems with long rotation periods. As such we independently determine stellar rotation periods using the KASOC data. We first consider the autocorrelation function (ACF) of the light curves, a method which has been shown to robustly retrieve periodic signals in stellar light curves (McQuillan, Aigrain & Mazeh 2013a). We follow a similar procedure to McQuillan, Mazeh & Aigrain (2014) in calculating ACF periods. Initially gaps in the data are filled with zeros, which does not affect the ACF
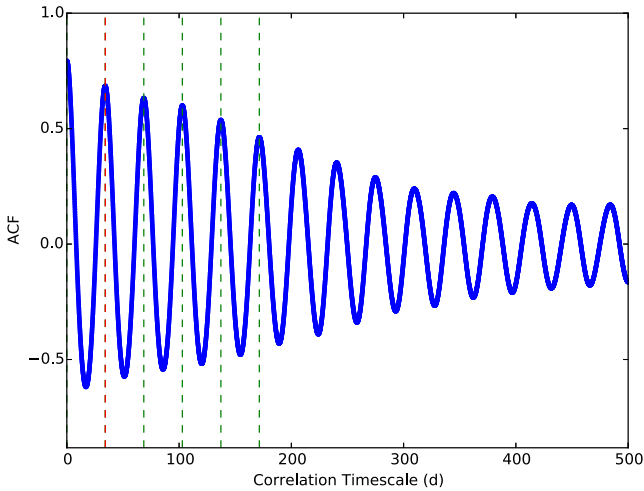
Figure 1. ACF for Kepler-186, calculated using the KASOC 50 d light curve. The rotation period is marked as the leftmost dashed line, with the peaks used to fit and extract this period also marked. The ACF has been smoothed by a Gaussian filter.

calculation. Data are then binned down by a factor of 4 cadences to speed processing. The ACF is then calculated via the equation:

$$r_k = \frac{\sum_{i=1}^{N-k}(x_i - \bar{x})(x_{i+k} - \bar{x})}{\sum_{i=1}^{N}(x_i - \bar{x})^2}, \qquad (1)$$

where the time series is given by $x_i(i = 1, \ldots, N)$, $\bar{x}$ is its mean, and the ACF value r_k is computed at successive lags k, with k being an integer multiple of the cadence. Extracting a period from this curve is non-trivial; we first smooth the curve using a Gaussian filter with a standard deviation the same as the maximum peak (to avoid adversely affecting this peak). The filter is truncated at 3.1σ. This leads to a curve of the form of Fig. 1. We then identify the first four harmonics of the first peak in the curve, and perform a linear fit to the locations of these peaks, as well as the first peak and the origin, giving six points overall. The final gradient and error of this fit then gives our ACF period and its error. Due to our small sample number, we are able to confirm the extracted period against the light curves themselves.

It is also useful to consider where this signal arises, as in some cases one noisy region of data can produce a false rotation signal. We therefore also perform a wavelet analysis (Torrence & Compo 1998), as has been used for *Kepler* data before (e.g. García et al. 2014; Mathur et al. 2014). This allows a study of the rotation signal in the time domain, although giving reduced resolution in frequency. Wavelet analysis consists of convolving a selected waveform with the data at each timestep, with the convolution performed repeatedly using a range of scales for the waveform. Each scale represents a different frequency. The power given by each convolution then produces a map of frequency against time. We use a custom-built code, centred around the open source PYTHON module 'wavelets'.[2] We use a Morlet wavelet, as has been previously used for stellar rotation applications. Rather than filling data gaps with zeros, which could bias the calculation, we use linear interpolation between the average of the 20 points on either side of each gap. For gaps greater

[2] https://github.com/aaren/wavelets

than 10 d, we continue to use zeros rather than assume a linear relation over an extended timespan. We use a scale resolution of 0.01, and unbias the resulting power spectrum as described in Liu, Liang & Weisberg (2007). An example wavelet plot is shown in Fig. 2.

To extract a period from the array of wavelet powers, the power is summed over the time axis, resulting in the global wavelet spectrum (GWS). The shape of a single period in the GWS is Gaussian, hence we approximate that the total GWS can be fit by the sum of several Gaussians (following the method of García et al. (2014). The fit is initialized with a Gaussian assigned to each peak in the GWS. Each Gaussian is given an initial amplitude of the GWS value at that peak location, with a standard deviation of a quarter of the peak's period. The fit is then found via least-squares optimization. The extracted period is then the peak location of the highest amplitude Gaussian, and the error the Half-Width-Half-Maximum of this peak. We note that the GWS has degraded resolution compared to a Fourier transform. It tends to give larger uncertainties, as can be seen in our results and as has been seen previously (e.g. García et al. 2014). This is partially because the GWS includes effects such as differential rotation, which can blur a periodic signal. However, following this same procedure for a test *Kepler*-length light curve consisting of a pure 30 d sinusoid without noise still resulted in a period error of ∼3 d, showing that the GWS produces an intrinsically large error even for clear periodicities. Hence in adopting final rotation values we use the ACF periods, but backed up by the wavelet spectrum. To ensure we do not pick up lower harmonics of the true rotation period due to attenuation, we adopt the period from the KASOC light curve with the shortest filter which is consistent with the 100 d KASOC light curve value (except for Kepler-62, see below).

The resulting stellar rotation periods are given in Table 4, and discussed in Section 4.1. The remaining wavelet plots are given in the appendix. We are able to obtain good rotation periods for six stars. In addition, Kepler-62 shows the rotation period given in Borucki et al. (2013) of near 39 d, but with a weak signal evident in only a few parts of the light curve, with only partial evidence backing this period up via visual inspection. We proceed using this period, but caution that it is unclear if this is the true rotation period. In addition, the KASOC 100 d light curve for Kepler-62 shows a 111 ± 9 d period, too long to be clearly confirmed given the *Kepler* 90 d quarter length but intriguing nevertheless. Kepler-174, Kepler-298, Kepler-442 and Kepler-443 give periods which are multiples of the 90 d quarter length and arise from artefacts associated with this. KOI-4427 gives a very weakly determined signal near 40 or 80 d. We are unable to distinguish between the two, and the signal arises from few regions of the light curve. Hence, we do not consider this as a conclusive period determination.

3.2 Stellar photometric activity

We next study the photometric activity of these stars. A number of methods for investigating activity with the *Kepler* light curves have been proposed, including the range (Basri et al. 2010; Basri, Walkowicz & Reiners 2013), S_{phot} (García et al. 2010) and more recently $S_{phot,k}$ (García et al. 2014; Mathur et al. 2014). The latter incorporates the stellar rotation period into the measurement of activity, an important link given that activity usually appears on time-scales of the stellar rotation period due to spot modulation. It has also been shown that the range can underestimate the true variability (García et al. 2014). As such we utilize $S_{phot,k}$ for this study. The choice of light curve used to calculate the activity is important. We trialled the PDC and each KASOC light curve, and
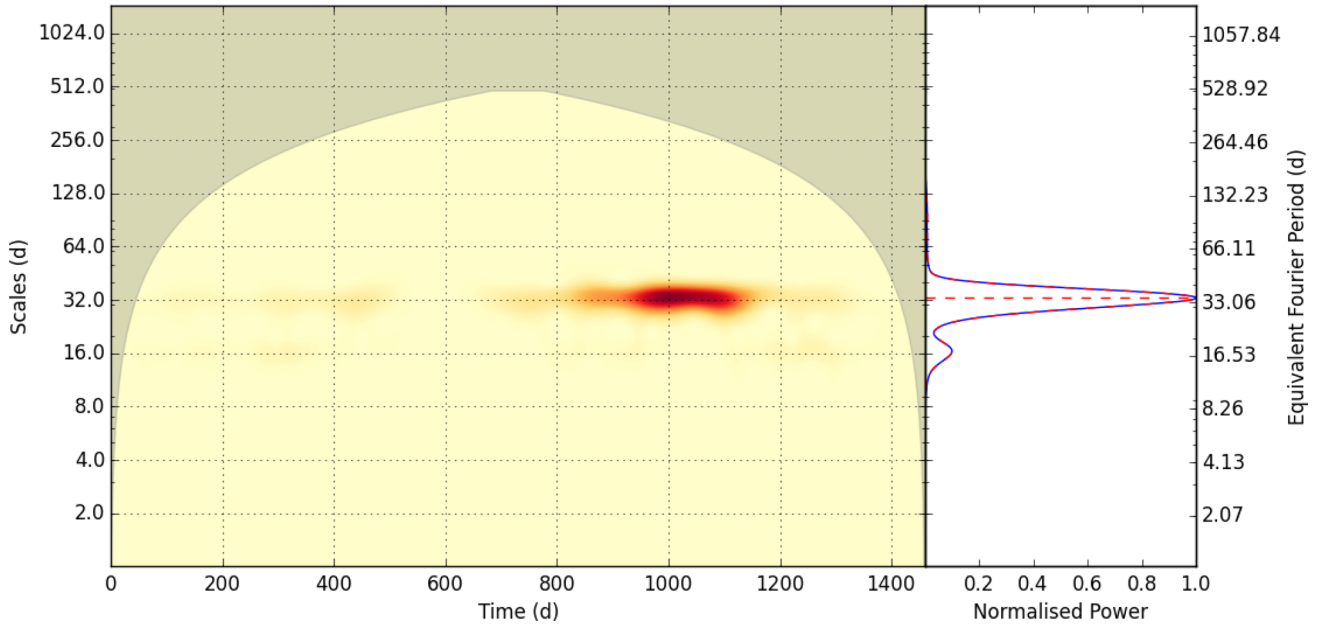
Figure 2. Contour wavelet plot for Kepler-186, calculated using the KASOC 50 d light curve. The GWS is plotted to the right and fit by a sum of Gaussians (curved dashed line). The horizontal dashed line shows the location of the maximum peak seen in the GWS. The rotation period is visible throughout the data, but becomes especially strong during an extended active region near 1000d from the data start. The P/2 harmonic can also be clearly seen.

found that as expected the measured activity is least for the PDC light curves due to the stronger attenuation of these generally longer period spot modulation signals. This trend continued through the KASOC light curves, with the highest activity measures found for the 100 d KASOC light curves. Finding the point at which this increased activity becomes due to instrumental effects which have not been removed is non-trivial. Given the ∼30 d rotation periods studied here, we chose to use the 50 d KASOC light curves for studying activity. We used these even for the two stars with shorter than 30 d rotation periods, for consistency. These light curves should preserve signals at the rotation periods of the stars well, without introducing the additional chance for instrumental noise of the 100 d KASOC light curves.

To calculate $S_{phot,k}$, the light curve is divided into successive windows of length k multiplied by the stellar rotation period. It has been shown that a robust indicator for magnetic activity is given when using $k = 5$ (Mathur et al. 2014), which we adopt here. The standard deviation of each window is taken, and the final measure $<S_{phot,5}>$ given by the mean of these. Windows containing less than 3/4 of the expected number of data points in a 5 rotation period timespan (due to, for example, gaps in the data) were not included. Where we could obtain no good rotation period for a star we performed this analysis using a period of 30 d, to allow some measure of the activity. Derived values for $<S_{phot,5}>$ are given in Table 4, and discussed in Section 4.2. By plotting the value of $S_{phot,5}$ for each window it is possible to track the activity of the star through the four years of *Kepler* data, an example of which is given in Fig. 3. We do not see any strong evidence for activity cycles in any of our targets. We also calculate the contrast for each star, as defined in (Mathur et al. 2014). The contrast is the ratio of the average value of $S_{phot,5}$ in the windows with greater than the global value of S_{phot} (i.e. the standard deviation of the whole data set) to that of the windows with lower than the global value, and gives a measure of the activity variation seen in the data.
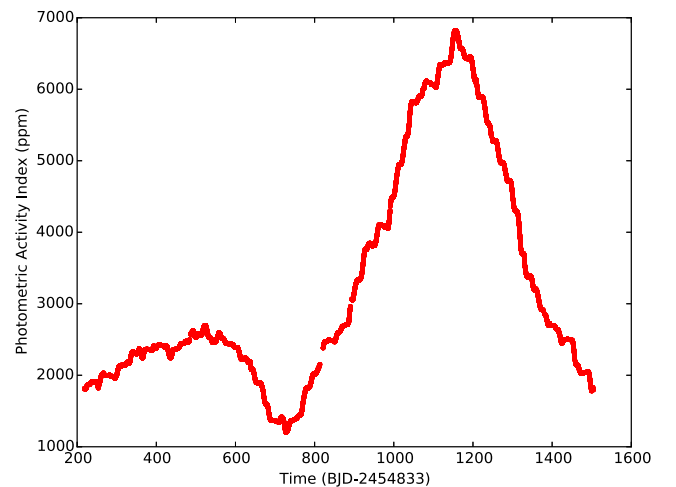
Figure 3. Photometric Activity Index $S_{phot,5}$ for Kepler-186, calculated using the ACF rotation period of 34.27 d. The active region evident in Fig. 2 is clearly visible.

3.3 Flares

We inspected each of the sample light curves (in long and short cadence) for evidence of flares, which have been detected in *Kepler* data previously for other stars (Maehara et al. 2012). For this study we utilized the PDC light curves in both long and short cadence, as flares occur on a time-scale of ∼a few cadences in the long cadence data, easily avoiding attenuation by the PDC detrending. For one star, Kepler-438, seven significant flares were found during the four years of *Kepler* data. Unfortunately no short cadence data are available for Kepler-438, but the flares are easily discernible in the long cadence data. Estimates of the flare energies were made

Table 2. Kepler-438 flares.

Quarter	Time BJD 2400000	Energy $\times 10^{32}$ erg
2	55 058.86	4 ± 2
3	55 141.14	7 ± 3
6	55 379.24	14 ± 6
8	55 572.92	8 ± 4
9	55 701.39	11 ± 5
10	55 799.08	6 ± 3
12	55 974.30	4 ± 2

using the flare amplitude, duration and luminosity, and were done in a similar manner to Shibayama et al. (2013).

The total energy of the flare can be estimated by integrating the bolometric luminosity of the flare over the flare duration:

$$E_{\text{flare}} = \int_{\text{flare}} L_{\text{flare}}(t)\, dt. \tag{2}$$

Assuming that the flare emission can be approximated by a black-body spectrum, the luminosity of the flare is given by

$$L_{\text{flare}} = \sigma_{\text{SB}} T_{\text{flare}}^4 A_{\text{flare}}, \tag{3}$$

where σ_{SB} is the Stefan–Boltzmann constant, T_{flare} is the effective temperature of the flare, and A_{flare} is the area covered by the flare. Since the ratio of the observed flare flux and stellar flux should be equal to the ratio of the flare luminosity and stellar luminosity, the following relationship can be used to estimate A_{flare} as a function of time:

$$\frac{\Delta F(t)}{F} = \frac{A_{\text{flare}}(t) \int R_\lambda B_{\lambda(T_{\text{flare}})} d\lambda}{\pi R_*^2 \int R_\lambda B_{\lambda(T_{eff})} d\lambda}, \tag{4}$$

where $\frac{\Delta F}{F}$ is the amplitude of the flare, λ is the wavelength, R_λ is the *Kepler* instrument response function, $B_{\lambda(T)}$ is the Planck function, and R_* is the stellar radius. This assumes that the star can also be approximated by a blackbody radiator. To find the flare amplitude as a function of time, the flare flux, $\Delta F(t)$, was found first by masking out the flare data points and interpolating linearly over those points, then calculating the differences between the flare flux values and the interpolated flux values. The flare flux was then normalized by the mean flux in the vicinity of the flare, with the flare masked out. This method limits the impact of an underlying trend in the light curve on the calculated energy. The stellar temperature (3748 ± 112 K) and radius ($0.520^{+0.038}_{-0.061}$ R$_\odot$) used to calculate the stellar luminosity were obtained by Muirhead et al. (2014) and Torres et al. (2015), respectively. The flare emission was assumed to be a blackbody spectrum at 9000 ± 500 K (Hawley & Fisher 1992; Hawley et al. 2003; Kretzschmar 2011). The energies of the seven detected flares are given in Table 2, and range from $(4 \pm 2) \times 10^{32}$ to $(1.4 \pm 0.6) \times 10^{33}$ erg, where flares with energies greater than 10^{33} erg are classified as superflares (Maehara et al. 2012). Solar flares typically do not reach beyond 10^{32} erg. Since this star was observed for four years, on average a large flare occurs every $\sim$200 d. The strongest superflare seen is shown in Fig. 4.

We did not detect any significant flares in any of the other sample light curves. While converting this to limits on flare energies is non-trivial, we estimate upper limits on any flares present in each light curve by considering a flare with peak flux 5 standard deviations above the mean light curve level for each star. The standard deviations used to set the test flare amplitude were obtained from flattened versions of the PDC light curves. Flattening was performed by fitting a third-order polynomial to 2 d windows surrounding suc-
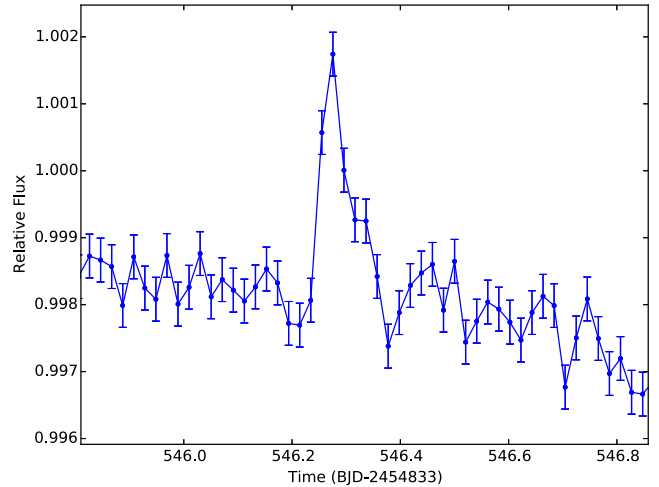
Figure 4. Superflare seen in quarter 6 of the Kepler-438 light curve, with an energy of $\sim 10^{33}$ erg.

Table 3. Upper limits of flare energies where the flare would not be detected above the noise level. LC = long cadence, SC = short cadence.

Star	Light curve	Energy limit $\times 10^{32}$ erg
Kepler-22	LC	6.5
Kepler-22	SC	4.4
Kepler-61	LC	3.1
Kepler-61	SC	2.2
Kepler-62	LC	4.5
Kepler-62	SC	3.2
Kepler-174	LC	5.4
Kepler-174	SC	4.1
Kepler-186	LC	1.4
Kepler-186	SC	1.0
Kepler-283	LC	7.6
Kepler-296	LC	2.8
Kepler-298	LC	7.9
Kepler-298	SC	5.6
Kepler-438	LC	1.6
Kepler-440	LC	4.0
Kepler-442	LC	5.6
Kepler-443	LC	24.0
KOI-4427	LC	6.9

cessive 0.2 d light curve segments. For each 0.2 d region, the fit is repeated 10 times, ignoring points more than 5σ discrepant from the previous fit. The polynomial is then removed from the 0.2 d region, and the process repeated for each 0.2 d region. These artificial flares were given durations of seven long cadences, a typical flare duration, and given rapid rise times and an exponential decay. Seven cadences is significantly shorter than the 2 d window used for fitting flattening polynomials, and hence such flares would not be affected by the flattening procedure. The energy such flares would have as calculated in the same way as for Kepler-438, i.e. the upper limit on individual flare energy in each light curve, is given in Table 3.

3.4 Mass-loss rates

Given that most of the stars considered here are cooler than the Sun, their habitable zones and hence the orbits of these planets are

closer to their host stars than that of the Earth. As such it is worth considering the state of the stellar wind, and particularly the impact it may have on each planet (see next section). To investigate the stellar mass-loss rates we turn to the model of Cranmer & Saar (2011), hereafter CS11. The CS11 model calculates stellar mass-loss rates considering Alfvén waves in the stellar atmosphere, with winds driven by hot coronal gas pressure and cool wave pressure in the extended chromosphere. The total mass-loss rate is found by combining these two effects.

The CS11 model has the significant advantage of requiring only observable stellar parameters, namely the stellar radius, mass, luminosity, metallicity and rotation period. As many of these parameters are used simply to calculate parameters such as effective temperature and surface gravity, we find it preferable to recast the model into a form with inputs of effective temperature, log g, metallicity, stellar radius and rotation period. In this form all inputs are direct observables, except the stellar radius which is generally derived from spectra. We chose to use this model over the commonly used Parker wind model (Parker 1958) due to the possibility of using these fundamental stellar parameters as inputs.

We use the input parameters given in Table 1 to populate the model. For stars where no good rotation period was found, we use a value of 30 d with an error of 1 d in order to estimate the mass-loss rate. Although the other inputs such as temperature are well determined, we stress that in these cases the mass-loss rates found are more of an estimate. In addition to mass-loss rates, the CS11 model outputs Rossby numbers, Ro (the ratio of rotation period to the convective turnover time, τ_c), which are given in Table 4. We do not give Rossby numbers for the stars with no good rotation period, as the Rossby number is a direct result of this period. The CS11 calculates τ_c and hence the Rossby number using the zero-age main sequence model of Gunn, Mitrou & Doyle (1998), see CS11 for a justification of this model over the various other methods of estimating τ_c (e.g. Barnes 2010; Landin, Mendes & Vaz 2010). Errors are calculated through a Monte Carlo procedure whereby the model was run for 10 000 iterations using normally distributed input variables. The mean and standard deviation of the output distributions give the values published here. We note that there can be significant discrepancies (up to ~25 per cent) between different methods of estimating τ_c, potential errors from which will feed into our Rossby numbers and hence values derived from them such as the gyrochronological ages. The errors given on these derived values do not incorporate these potential discrepancies in τ_c.

3.5 Stellar ages

We calculated gyrochronology ages using the formulation of Barnes (2010). We assume a value of 1.1 d for the rotation period at time $t = 0$ (following the calibrated Solar-mass model). Broad-band colour indices were taken from the AAVSO Photometric All-Sky Survey (Henden et al. 2012), accessed through the UCAC4 catalogue (Zacharias et al. 2013). The convective turnover time-scale τ_c was determined as described above. For each system we create Gaussian distributions for rotation period, τ_c, and $(B-V)$ colour, with mean and variance set to the known values and 1σ errors, respectively. These distributions were sampled 10^4 times, and the gyrochronological age calculated for each sampling. Final ages for each system were taken to be the median of the appropriate set of results, with 1σ uncertainties set to the values which encompassed the central 68.3 per cent of the data set.

Table 4. Host star derived parameters.

Star	P_{rot} (ACF) (d)	P_{rot} (GWS) (d)	$<S_{phot,5}>$ (ppm)	Contrast	Age (Gyr)	$\dot{M}$ ($M_\odot$ yr^{-1})	Rossby	log R_X	L_X ($L_{X,\odot}$)[e]	B_{ZDI} (G)	$R_{magneto}$ (planet) ($R_\oplus$)
Kepler-22	–	–	312	2.47	–	$(2.5 \pm 0.6) \times 10^{-14a}$	–	–	–	5[b]	8.7 (b)
Kepler-61	35.55 ± 0.38	34.8 ± 5.0	1680	1.45	7.5 ± 0.5	$(2.1 \pm 1.2) \times 10^{-16}$	0.91 ± 0.07	-4.89 ± 0.09	4.0 ± 1.3	2.4	12.7 (b)
Kepler-62	39.77 ± 0.44	37.3 ± 13.3	405	1.11	14.6 ± 0.6	$(1.4 \pm 0.2) \times 10^{-15}$	1.61 ± 0.06	-5.78 ± 0.12	1.2 ± 0.5	1.1	11.1 (e), 13.2 (f)
Kepler-174	–	–	445	1.47	–	$(2.6 \pm 1.4) \times 10^{-15a}$	–	–	–	5[b]	11.6(d)
Kepler-186	34.27 ± 0.07	33.8 ± 4.2	3270	2.32	6.0 ± 0.2	$(4.6 \pm 1.5) \times 10^{-17}$	0.75 ± 0.03	-4.69 ± 0.06	3.4 ± 0.8	3.1	19.2(f)
Kepler-283	18.27 ± 0.02	18.1 ± 2.2	2620	1.52	2.4 ± 0.1	$(1.7 \pm 1.0) \times 10^{-15}$	0.54 ± 0.03	-4.42 ± 0.05	13.4 ± 2.6	4.9	9.9(c)
Kepler-296	36.11 ± 0.13	35.0 ± 4.8	2800	1.36	6.6 ± 0.4	$(2.9 \pm 2.3) \times 10^{-17}$	0.78 ± 0.05	-4.73 ± 0.08	2.6 ± 1.1	2.9	13.7(e), 16.7(f)
Kepler-298	–	–	967	1.51	–	$(8.2 \pm 4.4) \times 10^{-16a}$	–	–	–	5[b]	10.7(d)
Kepler-438	37.04 ± 0.08	36.8 ± 4.5	3260	1.90	7.1 ± 0.4	$(3.2 \pm 1.8) \times 10^{-17}$	0.81 ± 0.05	-4.77 ± 0.08	2.8 ± 1.0	2.8	13.2(b)
Kepler-440	17.61 ± 0.02	17.3 ± 2.1	2420	1.37	2.0 ± 0.1	$(9.8 \pm 5.8) \times 10^{-16}$	0.47 ± 0.04	-4.33 ± 0.06	16.9 ± 4.4	5.9	9.6(b)
Kepler-442	–	–	736	1.50	–	$(7.7 \pm 2.3) \times 10^{-16a}$	–	–	–	5[b]	12.0(b)
Kepler-443	–	–	1250	1.25	–	$(2.4 \pm 0.6) \times 10^{-15a}$	–	–	–	5[b]	10.6(b)
KOI-4427	–	–	1410	1.44	–	$(6.3 \pm 3.6) \times 10^{-17a}$	–	–	–	5[b]	17.7(b)
Solar[c]	25.0	–	166.1	2.7	4.569	2×10^{-14}	1.577	-6.24	1	1.89–3.81	9.50(Earth)[d]

Notes. [a]Using rotation period of 30 d and error of 1 d.
[b]Example value used as no rotation period available.
[c]Solar values taken from Mathur et al. (2014), Vidotto et al. (2014), Cohen (2011), Bouvier & Wadhwa (2010) and references therein.
[d]Planetary magnetosphere extent for the Earth when calculated using the same method as the sample, for reference. The true standoff radius for the Earth varies between 9.7–10.3 $R_\oplus$.
[e]Using log $L_{X,\odot} = 20.05$ W. L_X values calculated from log R_X.
[f]Using log R_X values calculated from log R_X and values from Table 1.

3.6 Planetary magnetospheres

The Earth's magnetosphere is a crucial element to the habitability of the planet. It shields the surface from energetic particles and radiation, and prevents excessive loss of atmosphere. Magnetospheric protection is important in assessing exoplanet habitability (see e.g. See et al. 2014). We consider the extent of the hypothetical magnetospheres of our sample planets, given an assumed field strength the same as the Earth's. In this work, we are dealing with the radial distance of the magnetosphere from the planet's centre towards the star, the so-called magnetopause standoff distance. This distance is given where the planetary magnetospheric pressure balances the pressure from the star (Grie meier et al. 2004), as in

$$r_{MP} = \left(\frac{\mu_0 f_0^2 M_E^2}{8\pi^2 P_*} \right)^{1/6}, \tag{5}$$

where r_{MP} represents the magnetopause standoff distance, f_0 is a form factor accounting for the non-spherical shape of the planet's magnetic field, here set to 1.16, M_E is the Earth's magnetic moment, set to be $8 \times 10^{22} \mathrm{Am}^2$, and P_* represents the competing pressure from the star. The pressure on the planetary magnetosphere arises from stellar winds, as well as the magnetic and thermal pressures. We ignore the thermal pressure here, as the planets under consideration orbit relatively far from their host stars. The stellar wind pressure can be calculated from the mass-loss rate as

$$P_{wind}(r) = \frac{\dot{M} v_{esc}}{4\pi r^2} \tag{6}$$

at orbital distance r using the mass-loss rate of the CS11 model $\dot{M}$, the stellar escape velocity v_{esc} and following the prescription of See et al. (2014). At the orbital distances of our sample planets, the magnetic pressure can also be significant. This requires an estimate of the stellar magnetic fields. We use the empirically derived calibration between Rossby number and the large-scale structure magnetic field strength of Vidotto et al. (2014). As all of our sample stars fall in the unsaturated regime with $Ro > 0.1$ (e.g. James et al. 2000; Pizzolato et al. 2003; Wright et al. 2011) the average field strength scales with $< B_{ZDI} > \propto Ro^{-1.38 \pm 0.14}$. We fix this relation using the saturated field strength found for early M stars in Vidotto et al. (2014) of 50 G at $Ro = 0.1$. The average field strength is termed B_{ZDI}, as it is the component typically probed by the Zeeman Doppler Imaging technique.

The stellar magnetic field operates on both large and small scales; here the large-scale field is the dominant contributor, as the small-scale field falls off more rapidly with distance from the star (Lang et al. 2014). The Vidotto et al. (2014) calibration used gives the average large-scale magnetic field strength at the stellar surface. A commonly used method to extrapolate stellar magnetic fields is the PFSS (potential field source surface) technique, which assumes that field strength falls off as R^2 beyond the source-surface radius R_{SS} (see e.g. Vidotto et al. 2013). To calculate the average field strength $\langle B_{SS} \rangle$ at R_{SS}, we assume for this first-order estimate that the field follows a dipole structure between R_* and R_{SS}, hence $\langle B_{SS} \rangle = \langle B_{ZDI} \rangle (R_*/R_{SS})^3$. We assume that $R_{SS} = 2.5 R_*$, as in Vidotto et al. (2013). Following this chain of relations, the magnetic pressure at orbital radius $r > R_{SS}$ is given by

$$P_{magnetic}(r) = \frac{\langle B_{SS} \rangle^2}{2\mu_0} \left(\frac{R_{SS}}{r} \right)^4 \tag{7}$$

with all variables measured in SI units. It should be noted that stellar magnetic fields typically contain higher order multipoles than the simple dipole term, which will increase the rate of drop-off between the stellar and source-surface radii. Without detailed observations we cannot constrain these stellar magnetic fields further, hence we use the simple dipole approximation. The resulting field strengths will then be overestimated, which will result in magnetospheric standoff radii smaller than the true values. This approach is conservative – if the calculated magnetospheric standoff distances are large enough for the planets to maintain an Earth-like magnetosphere, then reduced magnetic pressure will only increase them.

In the cases where no good stellar rotation period (and hence Rossby number) is available, we assume a field $\langle B_{ZDI} \rangle = 5\,\mathrm{G}$ to allow an estimate of the magnetic pressure. Using the above mass-loss rates, Rossby numbers and scaling relations, we calculate planetary magnetospheric standoff radii through equation (5), with $P = P_{wind} + P_{magnetic}$. The resulting numbers are given in Table 4.

3.7 X-ray emission

It is possible to estimate the X-ray emission of these stars from the obtained Rossby numbers, using the relation of Mamajek & Hillenbrand (2008). All of our sample stars are in the unsaturated regime (e.g. Reiners, Basri & Browning 2009), meaning that the X-ray luminosity of the star falls off with increasing Rossby number. The relation follows

$$\log R_X = (-4.83 \pm 0.03) - (1.27 \pm 0.08)(Ro - 0.86), \tag{8}$$

where $R_X = L_X/L_{bol}$, the ratio of X-ray to bolometric luminosity, and Ro is the Rossby number. The resulting values for $\log R_X$ are given in Table 4. These stars all likely have X-ray luminosities too low to be easily observable with current technology, so in the absence of such data these estimates will prove useful in understanding the radiation environment of these planets.

3.8 Results

All of the results from the above sections are presented together in Table 4 for clarity.

4 DISCUSSION

4.1 Rotation periods

We find clear rotation signals for six stars, plus a present but less clear signal for Kepler-62. Each of these periods has been previously published in either the discovery papers or those cited below, but often in a number of different locations, using different methods and sets of data. Here we present what we believe to be the most comprehensive study of the rotation of these stars to date, using the entire *Kepler* data set, alternative detrending methods, and a combination ACF and wavelet analysis.

Previous studies of rotation in *Kepler* stars include McQuillan, Mazeh & Aigrain (2013b), who used the ACF technique, data from quarters 3–14 and give consistent periods to ours for Kepler-61, Kepler-186, Kepler-283 and Kepler-296. Rotation periods for these stars were also given by Walkowicz & Basri (2013) and Reinhold, Reiners & Basri (2013) using Lomb–Scargle periodogram techniques (Lomb 1976; Scargle 1982), although both of these studies give half the true rotation period for Kepler-61. Moreover, in Reinhold et al. (2013) while the periods given for the other three stars are close to ours, they are not consistent within the stated errors. Reinhold et al. (2013) also give periods for Kepler-440 and

KOI-4427. For KOI-4427, we find that their period (26.6 d) matches some active regions on our wavelet plot, but by no means represents a dominant or persistent signal. As such we cannot claim agreement for KOI-4427. None of our sample appear in the Nielsen et al. (2013) study of *Kepler* rotation periods.

It is interesting that all of our detected rotation periods are relatively long for *Kepler* stars, near the upper end of the range of periods found in McQuillan et al. (2014). This may be a result of observation bias, as longer rotation period stars tend to be less active and so in principle easier to detect transits within. However, as the next section shows, our sample stars are all quite active. The stars for which we do not detect rotation periods may be older, inactive stars, limiting the effect of any spot modulation which would allow us to detect their rotation signal. As such in terms of habitability, they may be preferred targets. In general, these stars have relatively low $\langle S_{\mathrm{phot,5}} \rangle$ values. In the more active cases, photometric variability can arise from sources other than starspots, such as in shorter time-scale 'flicker'.

4.2 Stellar photometric activity

The solar value of photometric activity when measured using $\langle S_{\mathrm{phot,5}} \rangle$ is 166.1 ppm, with a maximum value of 285.5 ppm (Mathur et al. 2014). Every star in our sample has a mean photometric activity level above the solar maximum, in some cases by an order of magnitude. They are also significantly more active than stars in similar studies, including Mathur et al. (2014) and García et al. (2014). This is to be expected, as our sample is dominated by K stars as opposed to the hotter targets studied previously (including the Sun). Cool stars are typically more active, but also represent easier targets for habitable planet detection due to their closer habitable zones. We note that the $S_{\mathrm{phot,k}}$ index does not consider stellar inclination, and as such if these stars were inclined to the line of sight their underlying photometric activity could be larger.

We do not see any strong evidence for magnetic cycles in our sample stars, which is unsurprising given the four year data baseline. This has the consequence that the activity indexes we measure are in effect 'snapshots' of the overall value, captured at a certain phase of the potential activity cycle. It is quite possible that activity will increase (or decrease) at other phases. Disentangling this effect would require more data spanning several years. Although it depends on target selection, there is the possibility of the *TESS* (Ricker et al. 2014) or *PLATO* (Rauer et al. 2014) satellites revisiting these targets at a later time.

It is unclear what direct effect activity can have on habitability, beyond the well-known difficulties it introduces in searching for small planets (e.g. Cegla et al. 2012; Haywood et al. 2014). The connection between photometric and spectroscopic activity is not clear, beyond a small sample studied by Bastien et al. (2014). It seems likely that increased photometric activity will lead to increased spectroscopic activity, and hence difficulty in securing radial velocities of low-mass rocky planets. Activity tends to be a marker of increased CMEs and flares, which can play a role in habitability in potentially stripping planetary atmospheres (e.g. Lammer et al. 2007). We investigate some of these stellar properties more directly in this work, but flares occurring at rates less than the four year *Kepler* data would not be seen. If energetic enough they could still pose some issue for their resident planets. Strongly active, flaring stars such as Kepler-438 can destroy atmospheric biomarkers in a planet's atmosphere (Grenfell et al. 2012, 2014), with implications for future searches for life.

4.3 Flares

The detection of superflares in the light curve of Kepler-438 could pose some interesting issues for habitability. An investigation into the impact of a powerful flare from an M dwarf on an Earth-like exoplanet in the habitable zone was made by Segura et al. (2010). They found that the increase in UV and X-ray emission associated with a flare would not have a significant impact on habitability, since X-rays could not penetrate beyond the upper atmosphere, and UV radiation at the surface would only reach slightly higher levels than on Earth. Any temperature increase due to ozone depletion would also be minor. In the absence of a planetary magnetic field, however, an increase in the flux of energetic charged particles associated with large flares could potentially be damaging to life.

On the Sun another phenomenon associated with flares is a CME, where a large amount of coronal material is expelled, often at high speeds (Gosling et al. 1976). The likelihood of a CME occurring increases with more powerful flares (Kahler 1992; Yashiro et al. 2005), however the relationship between flares and CMEs is complex, with some CMEs occurring without an associated flare (Munro et al. 1979). It is possible that CMEs occur on other stars that produce very energetic flares, which could have serious consequences for any close-in exoplanets without a magnetic field to deflect the influx of energetic charged particles. Since the habitable zone for M dwarfs is relatively close in to the star, any exoplanets could be expected to be partially or completely tidally locked. This would limit the intrinsic magnetic moments of the planet, meaning that any magnetosphere would likely be small. Khodachenko et al. (2007) found that for an M dwarf, the stellar wind combined with CMEs could push the magnetosphere of an Earth-like exoplanet in the habitable zone within its atmosphere, resulting in erosion of the atmosphere. Following on from this, Lammer et al. (2007) concluded that habitable exoplanets orbiting active M dwarfs would need to be larger and more massive than Earth, so that the planet could generate a stronger magnetic field and the increased gravitational pull would help prevent atmospheric loss.

Given Kepler-438b's relatively close orbit to its M dwarf host, the eventual effect of these flares is strongly dependent on the size and strength of its magnetic field. The magnetospheric extent calculated in Table 4 assumes an Earth-like magnetic moment, which may not be achievable for such a planet. If it has a higher than expected mass this would help prevent atmospheric mass-loss, but we cannot determine this with current observations. In any case, the high rate of strong flares (∼every 200 d) must be taken into account when considering Kepler-438b as an Earth-like planet.

In all other cases except Kepler-443, our calculations of upper limits on the flare energy rule out flares with greater than 10^{33} erg, the threshold for flares being classified as 'superflares'. Hence in these cases the situation may be much improved relative to Kepler-438. We reiterate however that the most significant factor determining the effect such flares and connected CMEs may have is the strength of the planetary magnetospheres, something almost completely unknown.

4.4 Planetary magnetospheres

Encouragingly all of our sample planets are able to sustain magnetospheres of near Earth size or greater, assuming Earth strength magnetic moments. Even the smallest magnetopause standoff distance in our sample (Kepler-440b, with $R_{\mathrm{magneto}} = 9.6\,\mathrm{R_{\oplus}}$, ignoring stars without well-defined Rossby numbers) is well above the Paleoarchaen Earth magnetopause standoff distance of ∼5 $\mathrm{R_{\oplus}}$ 3.4 Gyr

ago (Tarduno et al. 2010). This implies that subject to the generation of a planetary magnetic field similar to the Earth's in strength, magnetic protection should be effective for these planets at the present time. However, it is worth considering that magnetic activity and stellar winds are both expected to decline with age (e.g. Reiners & Mohanty 2012). As such earlier in the system's histories the extent of the magnetic field may not have been so large, and atmospheric stripping could become a possibility. However, See et al. (2014) find that for stars slightly more massive than M dwarfs (i.e. the K dwarfs which comprise the bulk of this sample) planetary magnetic protection is more effective over the stellar lifetime. Our results support this conclusion, albeit at only one epoch. In terms of the generation of planetary magnetic fields, Driscoll & Barnes (2015) studied tidal dissipation in potentially habitable exoplanets, and found that such dissipation can have significant effects on a planet's core. If the core solidifies, the planetary dynamo will become ineffective, making the generation of a strong planetary magnetic field impossible. Core-mantle interactions can also weaken the generated field.

4.5 Stellar mass-loss rates

Most of the mass-loss rates reported in Table 4 are an order of magnitude or more lower than the solar value. Calculating the solar mass-loss rate using the CS11 model gives a value of $3.6 \times 10^{-14} M_\odot \ \mathrm{yr}^{-1}$, a slightly overestimated but reasonable result which supports the validity of the model. The lower values found for our sample stars are a result of their longer rotation periods as compared to the Sun. The derived mass-loss rates here are again often orders of magnitude lower than measured mass-loss rates for other stars (see the list of such measurements in CS11, and references therein). We note the small number of measured rates however, which as a sample have shorter rotation periods and hence larger Rossby numbers. If the true mass-loss rates of our sample stars are in fact higher, it will decrease the calculated planetary magnetopause standoff distances.

4.6 X-ray emission

All of our calibrated values for X-ray emission are higher than the solar value of $\log R_X = -6.24$ (Judge, Solomon & Ayres 2003), generally by orders of magnitude. This is to be expected for these later type stars. Given that the habitable zone of such cooler stars lies closer to the star, the reduced planetary orbital distance and increased X-ray emission will lead to a significantly higher incident flux of X-rays at the planet's surface, though in the presence of an atmosphere much of this would be attenuated before reaching the surface (Cnossen et al. 2007). Higher stellar X-ray flux is also associated with increased CME and planetary atmospheric stripping (Lammer et al. 2007), seriously affecting habitability. We expect these values to be useful in future modelling of the *Kepler* habitable exoplanet atmospheres.

5 CONCLUSION

We have presented a study of the light curves of the host stars of the most Earth-like *Kepler* planets known to date. We also present the detection of superflares on Kepler-438, the most Earth-like exoplanet known to date according to the ESI, with energetic flares occurring every ∼200 d. These may have strong consequences for planetary habitability, depending on the strength of the planet's magnetosphere. We have also presented the most comprehensive

study of stellar rotation on these stars to date, using the whole *Kepler* data set as well as an alternative detrending method. Using these rotation periods and previously published stellar parameters, we have calculated the photometric activity indices, mass-loss rates, gyrochronological ages, Rossby numbers, X-ray fluxes and magnetic pressure exerted by these stars. This leads to an estimate of the magnetospheric standoff distance for the planets, assuming Earth-like magnetospheres, showing that in principle these planets could all maintain an Earth-sized magnetosphere. We stress that the parameters not calculated directly from the light curves (i.e. mass-loss rates, ages, Rossby numbers, X-ray fluxes and magnetic field values) are model based estimates, and should be treated as such. All of the directly and indirectly calculated parameters may come to bear in assessing planetary habitability, and in future detailed studies of these systems.

### REFERENCES

Ballard S. et al., 2013, ApJ, 773, 98
Barclay T., Quintana E. V., Adams F. C., Ciardi D. R., Huber D., Foreman-Mackey D., Montet B. T., Caldwell D., 2015, ApJ, 809, 7
Barnes S. A., 2010, ApJ, 722, 222
Basri G. et al., 2010, AJ, 141, 20
Basri G., Walkowicz L. M., Reiners A., 2013, ApJ, 769, 37
Bastien F. A. et al., 2014, AJ, 147, 29
Borucki W. J. et al., 2010, Science, 327, 977
Borucki W. J. et al., 2012, ApJ, 745, 120
Borucki W. J. et al., 2013, Science, 340, 587
Bouvier A., Wadhwa M., 2010, Nature Geosci., 3, 637
Cegla H. M. et al., 2012, MNRAS, 421, L54
Chen J., Kunkel V., 2010, ApJ, 717, 1105
Cnossen I., Sanz-Forcada J., Favata F., Witasse O., Zegers T., Arnold N. F., 2007, J. Geophys. Res., 112, E02008
Cohen O., 2011, MNRAS, 417, 2592
Cohen O., Drake J. J., Glocer A., Garraffo C., Poppenhaeger K., Bell J. M., Ridley A. J., Gombosi T. I., 2014, ApJ, 790, 57
Cohen O., Ma Y., Drake J. J., Glocer A., Garraffo C., Bell J. M., Gombosi T. I., 2015, ApJ, 806, 41
Cranmer S. R., Saar S. H., 2011, ApJ, 741, 54 (CS11)
Driscoll P. E., Barnes R., 2015, Astrobiology, 15, 739
France K., Linsky J. L., Parke Loyd R. O., 2014, Ap&SS, 354, 3
García R. A., Mathur S., Salabert D., Ballot J., Régulo C., Metcalfe T. S., Baglin A., 2010, Science, 329, 1032
García R. A., Ceillier T., Mathur S., Salabert D., 2013, in Shibahashi H., Lynas-Gray A. E., eds, ASP Conf. Ser. Vol. 479, Progress in Physics of the Sun and Stars: A New Era in Helio- and Asteroseismology. Astron. Soc. Pac., San Francisco, p. 129
García R. A. et al., 2014, A&A, 572, A34
Gosling J. T., Hildner E., MacQueen R. M., Munro R. H., Poland A. I., Ross C. L., 1976, Sol. Phys., 48, 389

Grenfell J. L. et al., 2012, Astrobiology, 12, 1109
Grenfell J. L., Gebauer S., von Paris P., Godolt M., Rauer H., 2014, Planet. Space Sci., 98, 66
Grie meier J. M. et al., 2004, A&A, 425, 753
Gunn A. G., Mitrou C., Doyle J. G., 1998, MNRAS, 296, 150
Handberg R., Lund M. N., 2014, MNRAS, 445, 2698
Hawley S. L., Fisher G. H., 1992, ApJS, 78, 565
Hawley S. L. et al., 2003, ApJ, 597, 535
Haywood R. D. et al., 2014, MNRAS, 443, 2517
Hempelmann A., Schmitt J. H. M. M., Schultz M., Ruediger G., Stepien K., 1995, A&A, 294, 515
Henden A. A., Levine S. E., Terrell D., Smith T. C., Welch D., 2012, J. Am. Assoc. Var. Star Obs., 40, 430
James D. J., Jardine M. M., Jeffries R. D., Randich S., Collier Cameron A., Ferreira M., 2000, MNRAS, 318, 1217
Johnson M. C., Redfield S., Jensen A. G., 2015, ApJ, 807, 162
Judge P. G., Solomon S. C., Ayres T. R., 2003, ApJ, 593, 534
Kahler S. W., 1992, ARA&A, 30, 113
Kasting J., 1993, Icarus, 101, 108
Khodachenko M. L. et al., 2007, Astrobiology, 7, 167
Koch D. G. et al., 2010, ApJ, 713, L79
Kretzschmar M., 2011, A&A, 530, A84
Lammer H. et al., 2007, Astrobiology, 7, 185
Landin N. R., Mendes L. T. S., Vaz L. P. R., 2010, A&A, 510, A46
Lang P., Jardine M., Morin J., Donati J. F., Jeffers S., Vidotto A. A., Fares R., 2014, MNRAS, 439, 2122
Liu Y., Liang X. S., Weisberg R. H., 2007, J. Atmos. Ocean. Technol., 24, 2093
Lomb N. R., 1976, Ap&SS, 39, 447
McQuillan A., Aigrain S., Mazeh T., 2013a, MNRAS, 432, 1203
McQuillan A., Mazeh T., Aigrain S., 2013b, ApJ, 775, L11
McQuillan A., Mazeh T., Aigrain S., 2014, ApJS, 211, 24
Maehara H. et al., 2012, Nature, 485, 478
Mamajek E. E., Hillenbrand L. A., 2008, ApJ, 687, 1264
Mathur S. et al., 2014, A&A, 562, A124
Muirhead P. S. et al., 2014, ApJ, 213, 5
Munro R. H., Gosling J. T., Hildner E., MacQueen R. M., Poland A. I., Ross C. L., 1979, Sol. Phys., 61, 201

Nielsen M. B., Gizon L., Schunker H., Karoff C., 2013, A&A, 557, L10
Parker E. N., 1958, ApJ, 128, 664
Pizzolato N., Maggio A., Micela G., Sciortino S., Ventura P., 2003, A&A, 397, 147
Quintana E. V. et al., 2014, Science, 344, 277
Rauer H. et al., 2014, Exp. Astron., 38, 249
Reiners A., Mohanty S., 2012, ApJ, 746, 43
Reiners A., Basri G., Browning M., 2009, ApJ, 692, 538
Reinhold T., Reiners A., Basri G., 2013, A&A, 560, A4
Ricker G. R. et al., 2014, in Oschmann J. M., Clampin M., Fazio G. G., MacEwen H. A., eds, Proc. SPIE Conf. Ser. Vol. 9143, Space Telescopes and Instrumentation 2014: Optical, Infrared, and Millimeter Wave. SPIE, Bellingham, p. 914320
Rowe J. F. et al., 2014, ApJ, 784, 45
Scargle J. D., 1982, ApJ, 263, 835
Schulze-Makuch D. et al., 2011, Astrobiology, 11, 1041
See V., Jardine M., Vidotto A. A., Petit P., Marsden S. C., Jeffers S. V., do Nascimento J. D., Jr, 2014, A&A, 570, A99
Segura A., Walkowicz L. M., Meadows V., Kasting J., Hawley S., 2010, Astrobiology, 10, 751
Shibayama T. et al., 2013, ApJ, 209, 5
Smith J. C. et al., 2012, PASP, 124, 1000
Stumpe M. C. et al., 2012, PASP, 124, 985
Tarduno J. A. et al., 2010, Science, 327, 1238
Torrence C., Compo G. P., 1998, Bull. Am. Meteorol. Soc., 79, 61
Torres G. et al., 2015, ApJ, 800, 99
van Saders J. L., Pinsonneault M. H., 2013, ApJ, 776, 67
Vidotto A. A., Jardine M., Morin J., Donati J. F., Lang P., Russell A. J. B., 2013, A&A, 557, A67
Vidotto A. A. et al., 2014, MNRAS, 441, 2361
Walkowicz L. M., Basri G. S., 2013, MNRAS, 436, 1883
Wright N. J., Drake J. J., Mamajek E. E., Henry G. W., 2011, ApJ, 743, 48
Yashiro S., Gopalswamy N., Akiyama S., Michalek G., Howard R. A., 2005, J. Geophys. Res., 110, A12S05
Zacharias N., Finch C. T., Girard T. M., Henden A., Bartlett J. L., Monet D. G., Zacharias M. I., 2013, AJ, 145, 44
Zendejas J., Segura A., Raga A. C., 2010, Icarus, 210, 539

APPENDIX A: WAVELET PLOTS

Here, we show the wavelet plots associated with the light curves used to produce the periods given in Table 4. For stars where no conclusive period was given, the wavelet plot of the 100 d KASOC light curve is shown.

[h]
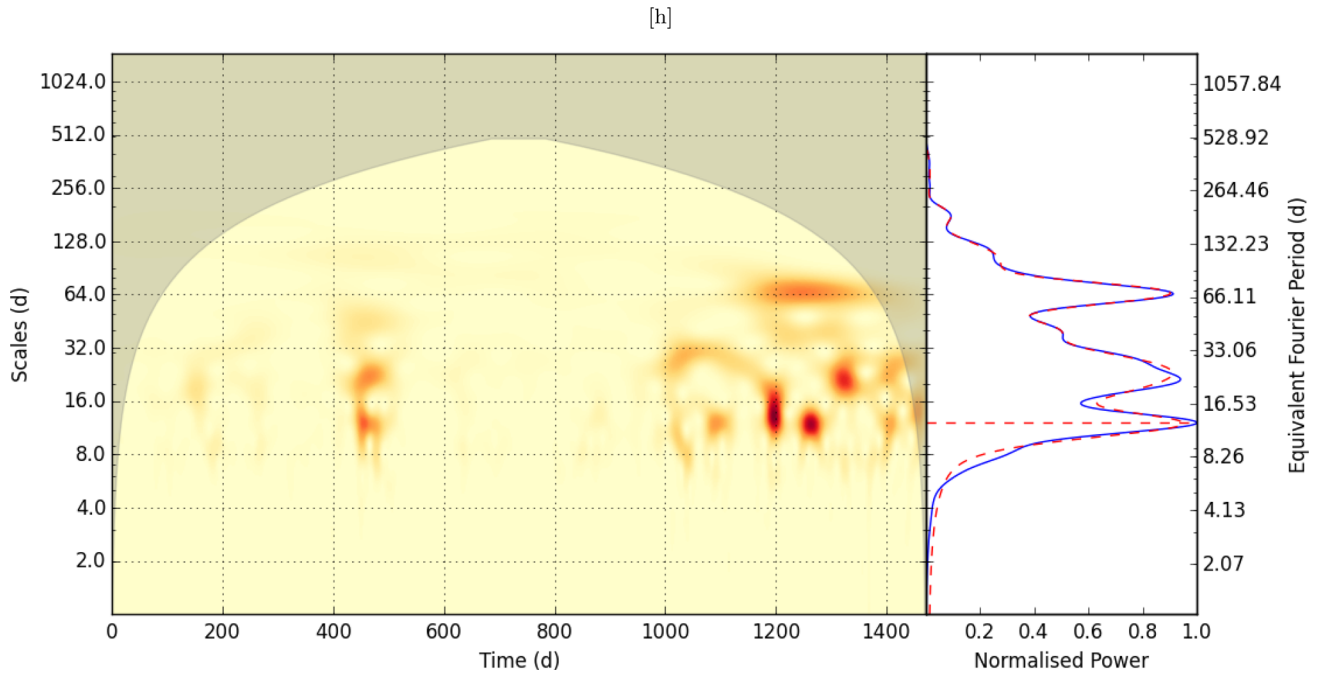
Figure A1. Contour wavelet plot for Kepler-22, calculated using the KASOC 100 d light curve. The GWS is plotted to the right and fit by a sum of Gaussians (dashed line). The horizontal dashed line in the GWS represents the maximum peak seen.
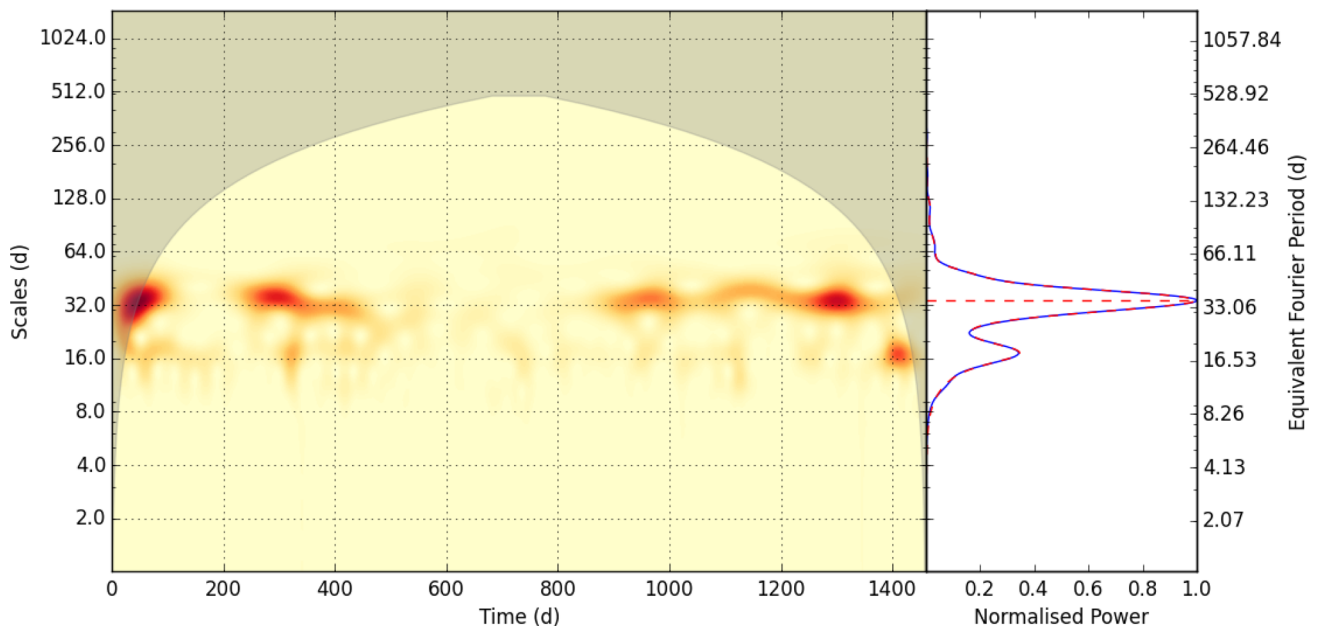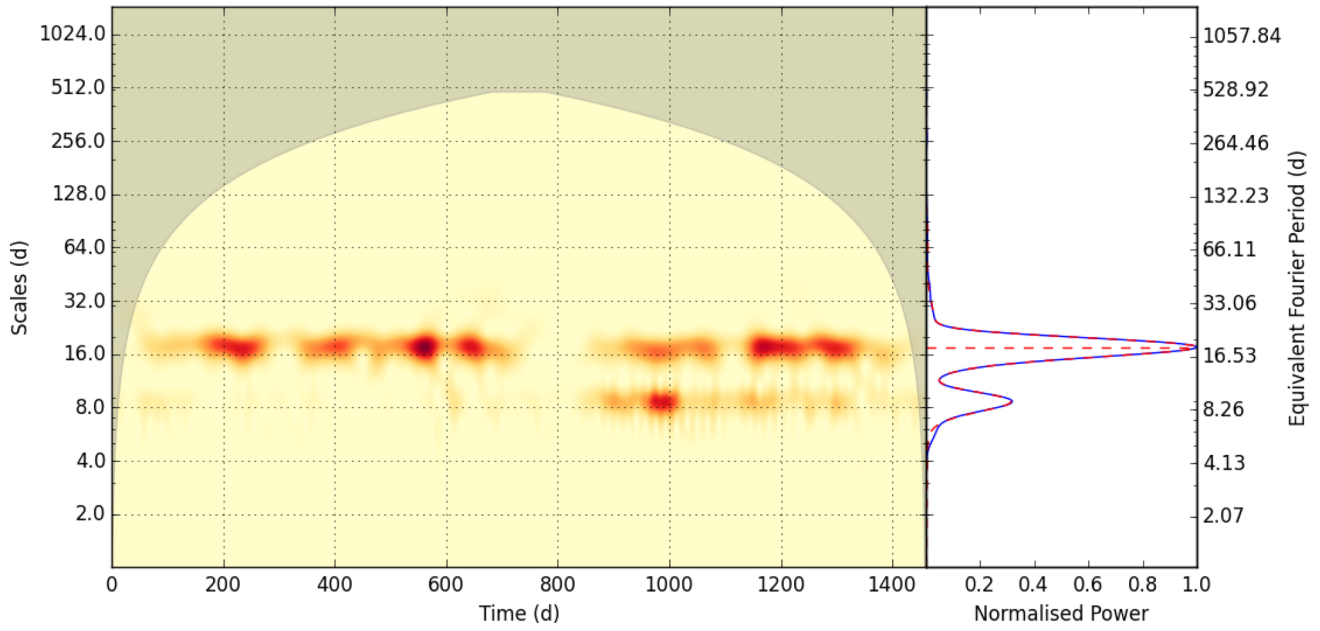

Figure A2. Contour wavelet plot for Kepler-61, calculated using the KASOC 50 d light curve. See Fig. A1 for description.
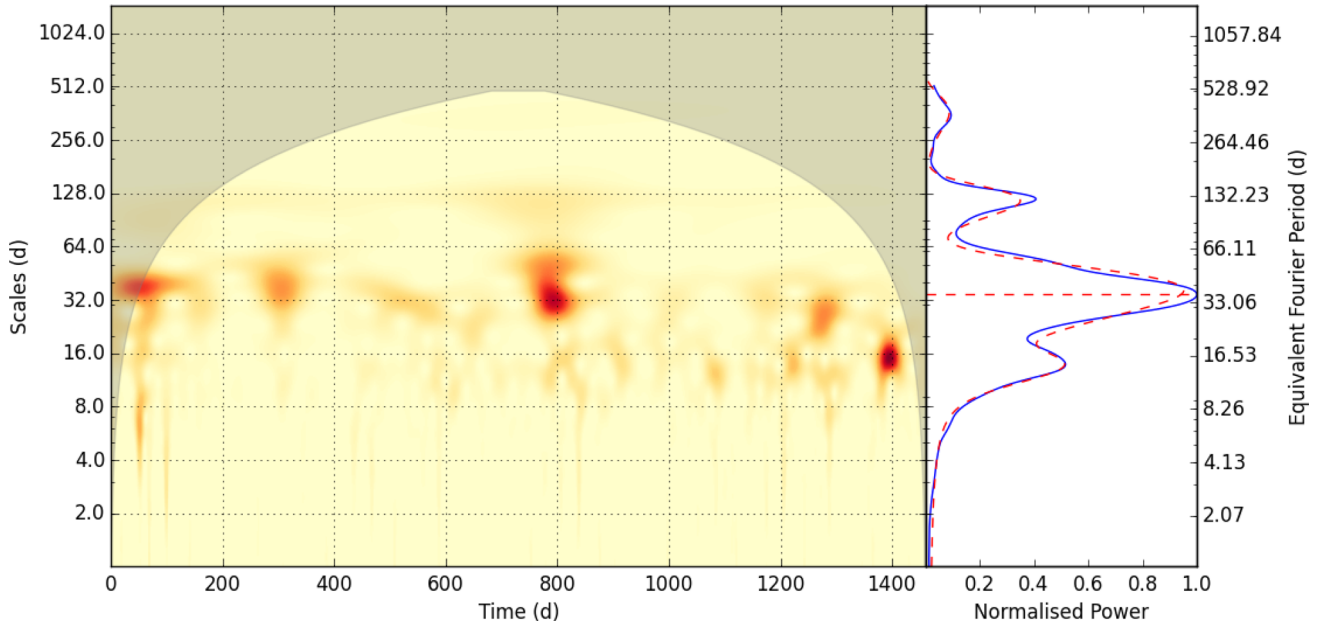
Figure A3. Contour wavelet plot for Kepler-62, calculated using the KASOC 50 d light curve. See Fig. A1 for description.
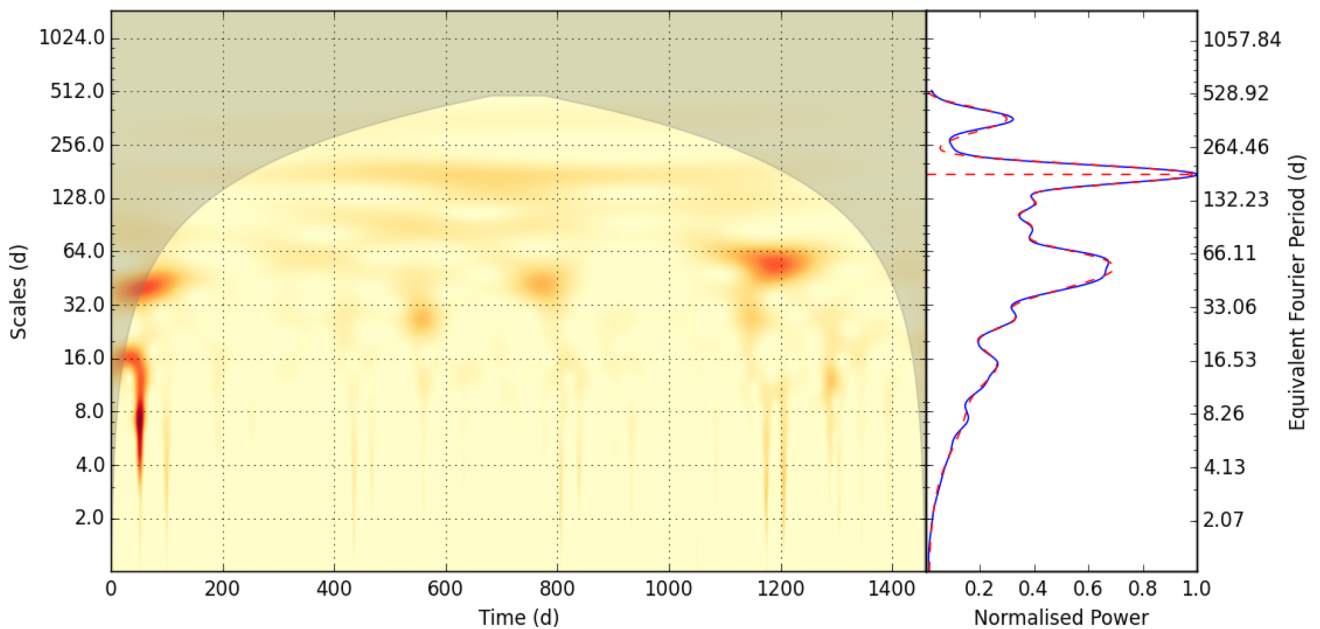
Figure A4. Contour wavelet plot for Kepler-174, calculated using the KASOC 100 d light curve. See Fig. A1 for description. For Kepler-174 data points near gaps of greater than 0.8 d were cut due to excessive gap related discontinuities.
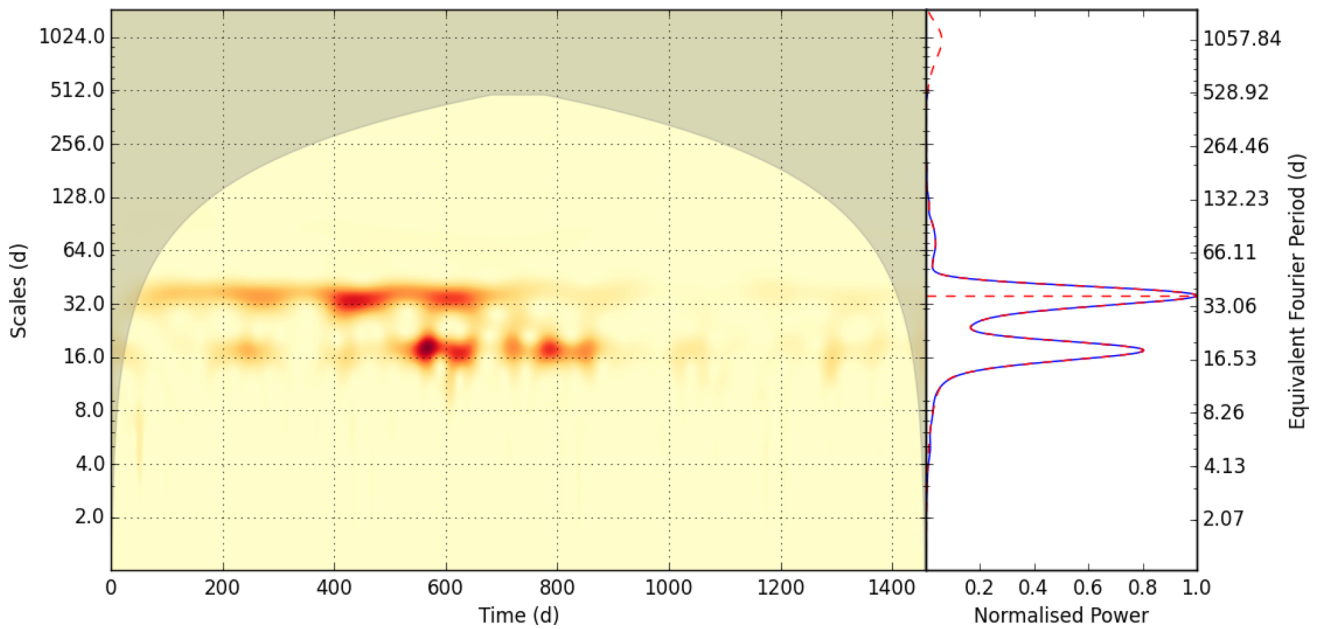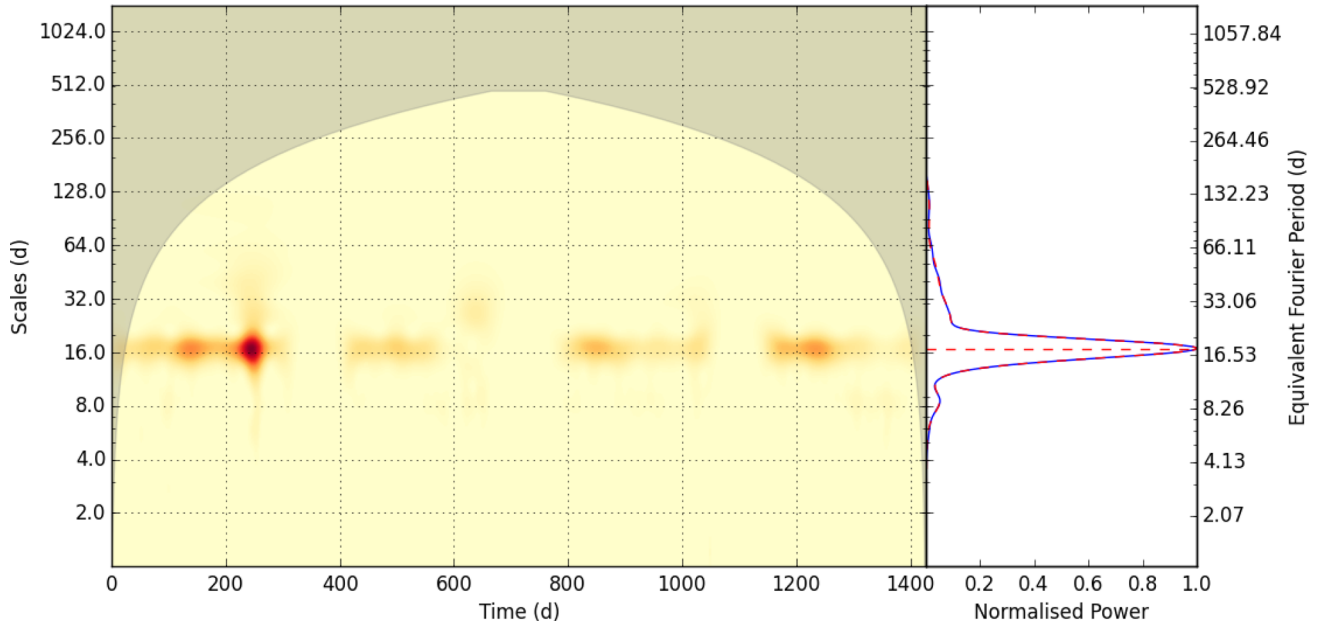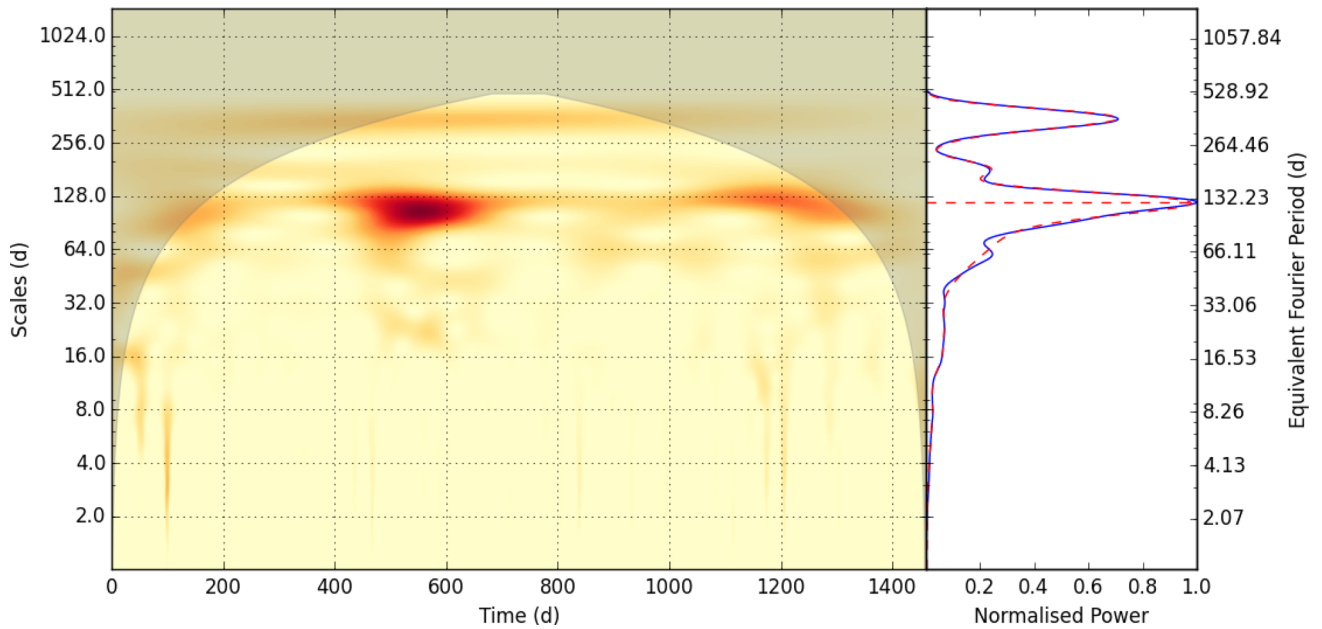
Figure A5. Contour wavelet plot for Kepler-283, calculated using the KASOC 30 d light curve. See Fig. A1 for description.
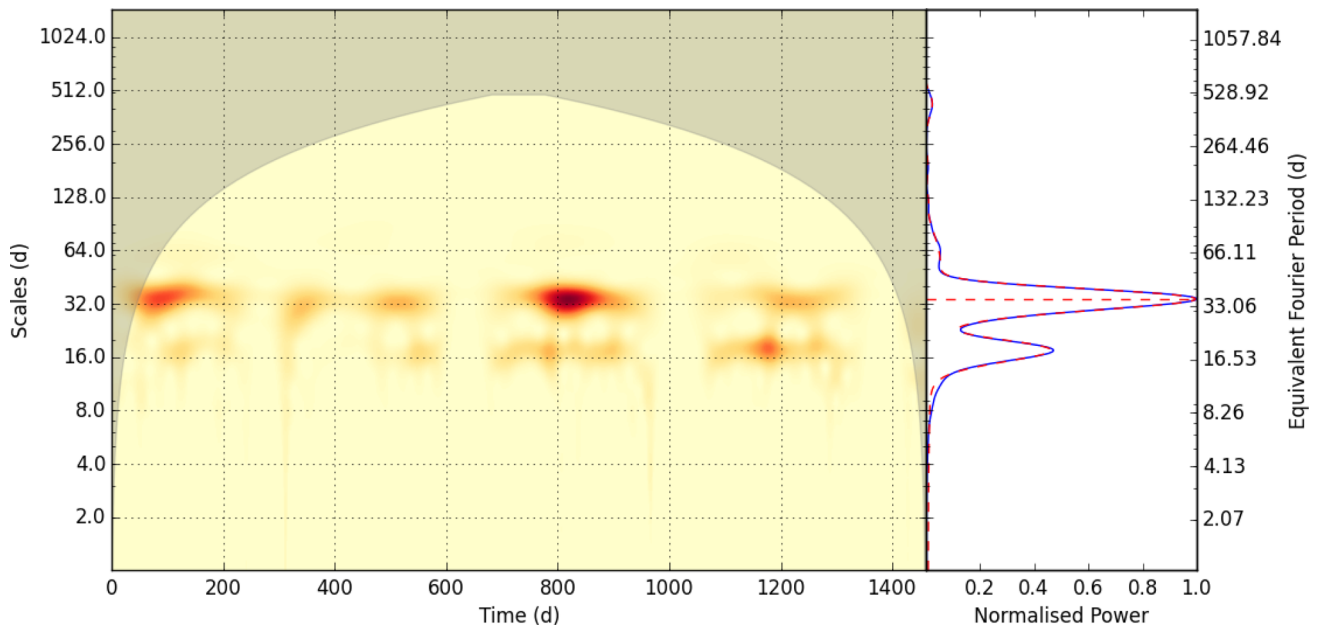
Figure A6. Contour wavelet plot for Kepler-296, calculated using the KASOC 30 d light curve. See Fig. A1 for description.
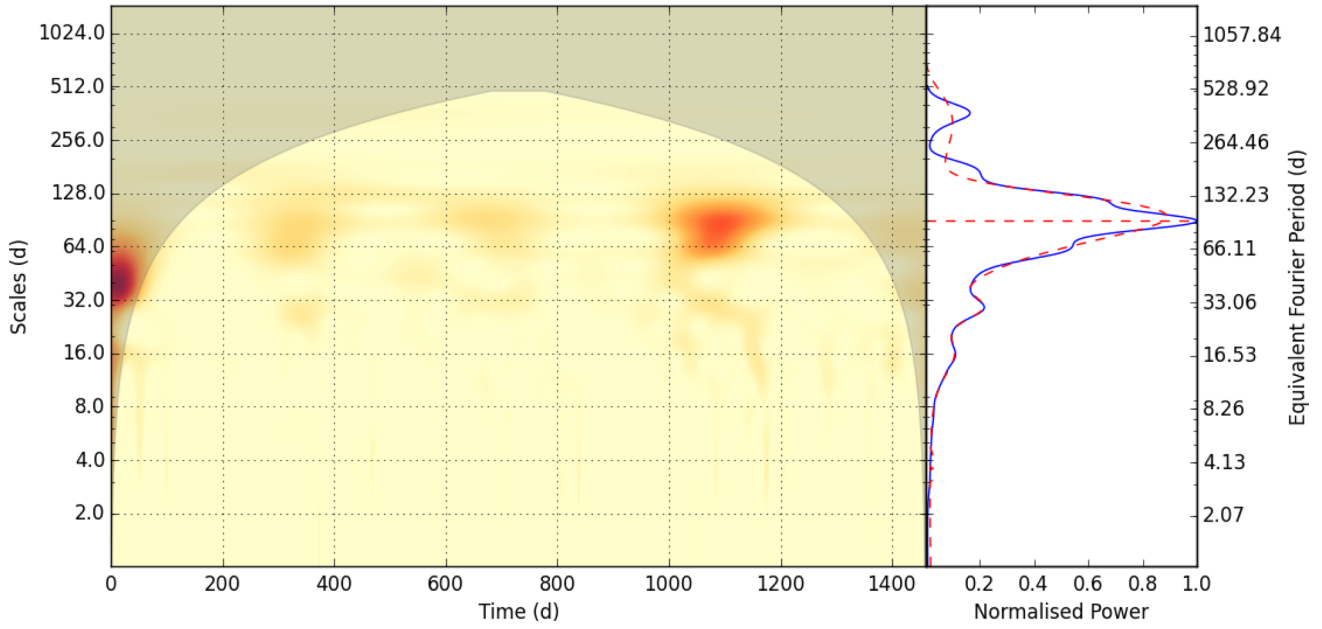
Figure A7. Contour wavelet plot for Kepler-298, calculated using the KASOC 100 d light curve. See Fig. A1 for description.

Figure A8. Contour wavelet plot for Kepler-438, calculated using the KASOC 30 d light curve. See Fig. A1 for description.
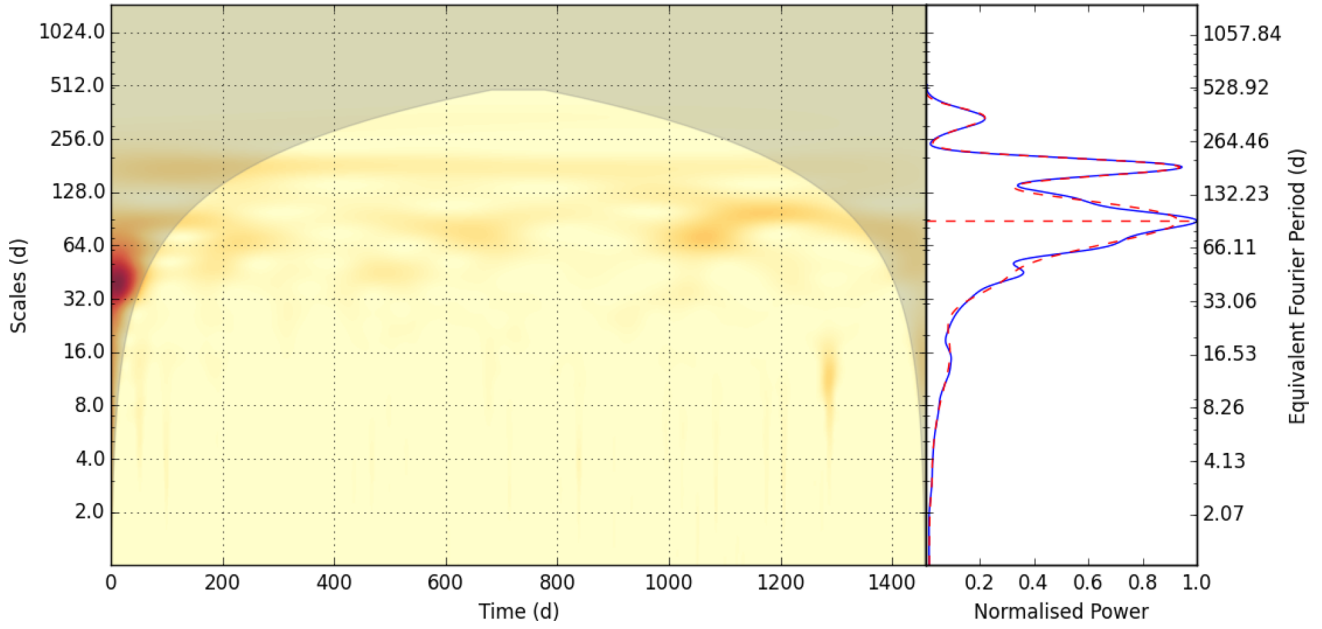
Figure A9. Contour wavelet plot for Kepler-440, calculated using the KASOC 30 d light curve. See Fig. A1 for description.
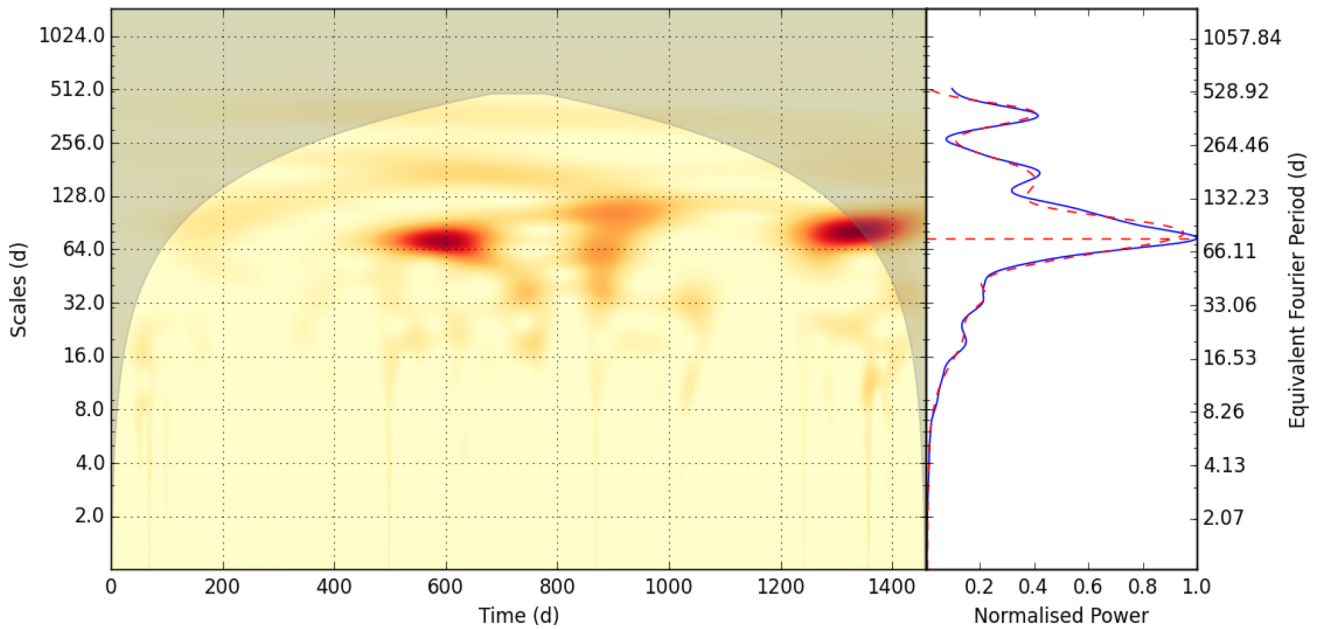

Figure A10. Contour wavelet plot for Kepler-442, calculated using the KASOC 100 d light curve. See Fig. A1 for description.

Figure A11. Contour wavelet plot for Kepler-443, calculated using the KASOC 100 d light curve. See Fig. A1 for description.

Figure A12. Contour wavelet plot for KOI-4427, calculated using the KASOC 100 d light curve. See Fig. A1 for description.

This paper has been typeset from a TEX/LATEX file prepared by the author.